Science
AAAS

Hierarchical Self-Assembly of F-Actin and Cationic Lipid Complexes: Stacked Three-Layer Tubule Networks

Gerard C. L. Wong, *et al.*

Science **288**, 2035 (2000);
DOI: 10.1126/science.288.5473.2035

Science (print ISSN 0036-8075; online ISSN 1095-9203) is published weekly, except the last week in December, by the American Association for the Advancement of Science, 1200 New York Avenue NW, Washington, DC 20005.

of the orbit of Magnya subjected to the perturbations of the jovian planets for 70 My. Magnya is not presently involved in any resonance, and its motion is regular over the computed time span. The long-term behavior of the characteristic angle of the $g + s - g_5 - s_7$ secular resonance is a prograde circulation with a period ~ 1.37 My. The proximity of the asteroid to the secular resonance involving the longitudes of the perihelion and of the node affects the asteroid's e and i and may explain their high values.

About 200 asteroids have been observed in the Magnya region, and about 20 of these asteroids are presently involved in some mean-motion resonances showing chaotic behavior. The majority of the actual asteroids appear to avoid the chaotic domains that indicate the possible existence of important diffusion processes associated with the mean-motion resonances.

Our spectra and orbital dynamic simulations suggest that after the breakup of Magnya's parent body, the fragments were scattered around a wide region depending on physical parameters such as the impact energy and the strength of the parent body and the sizes and velocities of the ejected fragments. The fragments that fell into the chaotic zones were slowly diffused out of the region, whereas Magnya, and possibly some other fragments, remained in stable orbits outside the zones of chaotic motion.

Geochemical data imply that the HEDs are derived from a single parent body (*16*, *17*). The spectral evidence and the abundance of apparent Vesta fragments in the resonance-rich inner solar system suggest that Vesta is the HED parent body (*2*–*9*). However, the transport time of main-belt asteroids to near-Earth space through the 3:1 and ν_6 resonances is of shorter duration than the cosmic ray exposure time of meteorites. Although slower diffusion processes such as a multitude of weak resonances (*23*–*25*) may solve this problem for all meteorite types including the HEDs, fragments from the Magnya parent body would also have long exposure times. However, considering our current understanding of the much lower delivery efficiency from the outer belt relative to the inner belt, we do not consider Magnya to be a likely alternative source to Vesta for the HED meteorites.

References and Notes

1. J. T. Wasson and G. W. Wetherill, in *Asteroids*, T. Gehrels, Ed. (Univ. of Arizona Press, Tucson, AZ, 1979), pp. 926–974.
2. T. B. McCord, J. B. Adams, T. V. Johnson, *Science* **168**, 1445 (1970).
3. L. A. McFadden, T. B. McCord, C. Pieters, *Icarus* **31**, 439 (1977).
4. R. P. Binzel *et al.*, *Icarus* **128**, 95 (1997).
5. J. G. Williams, in *Asteroids II*, R. P. Binzel, T. Gehrels, M. S. Matthews, Eds. (Univ. of Arizona Press, Tucson, AZ, 1989), pp. 1034–1072.
6. V. Zappalà, P. Bendjoya, A. Cellino, P. Farinella, C. Froeschlé, *Icarus* **116**, 291 (1995).
7. R. P. Binzel and S. Xu, *Science* **260**, 186 (1993).
8. T. H. Burbine and R. P. Binzel, *Bull. Am. Astron. Soc.* **29**, 964 (1997).
9. P. C. Thomas *et al.*, *Science* **277**, 1492 (1997).
10. D. Lazzaro, C. A. Angeli, M. Florczak, M. A. Barucci, M. Fulchignoni, *Bull. Am. Astron. Soc.* **29**, 975 (1997).
11. The observations were obtained at the ESO (La Silla, Chile) under an agreement with the Conselho Nacional de Desenvolvimento Científico e Tecnológico (CNPq)–Observatório Nacional (Brazil). We used the 1.52-m telescope equipped with a Boller and Chivens spectrograph and a charge-coupled device (CCD) (2048 × 2048 pixels) with a readout noise of ±7 electrons and a grating of 225 grooves/mm, with a dispersion of 330 Å/mm in the first order. The CCD has a square 15-μm pixel, giving a dispersion of about 5 Å/pixel in the wavelength direction. The useful spectral range is about $4900 < \lambda < 9200$ Å with a full width at half maximum of 10 Å. The spectra were taken through a 5-arc sec slit oriented in the east-west direction. The spectral data reduction was performed with the IRAF package and the classical procedure with averaged bias and flat fields, wavelength calibration with a He-Ar lamp (obtained several times during each night), and correction from air mass with the mean extinction curve of La Silla.
12. The instrumentation and observing procedures are described by S. J. Bus *et al.* (in preparation). Both instruments are long-slit grism spectrographs that use CCD array detectors providing about 30 arc sec of spatial resolution over their full range of spectral sensitivity. The spectrum of the sky background is recorded simultaneously with that of the object. Sky subtraction and spectral summing were accomplished with the IRAF package produced by the National Optical Astronomical Observatories.
13. F. Migliorini *et al.*, *Meteorit. Planet. Sci.* **32**, 903 (1997).
14. E. F. Tedesco, Planetary Data System—Small Bodies Node (PDSSBN), M. A'Hearn (University of Maryland, College Park, MD) (available at pdssbn.astro.umd.edu).
15. B. H. Zellner *et al.*, *Icarus* **128**, 83 (1997).
16. M. J. Drake, in *Asteroids*, T. Gehrels, Ed. (Univ. of Arizona Press, Tucson, AZ, 1979), pp. 765–782.
17. G. J. Consolmagno and M. J. Drake, *Geochim. Cosmochim. Acta* **41**, 1271 (1977).
18. E. R. D. Scott *et al.*, in *Asteroids II*, R. P. Binzel, T. Gehrels, M. S. Matthews, Eds. (Univ. of Arizona Press, Tucson, AZ, 1989), pp. 701–739.
19. A. Milani and Z. Knezević, *Icarus* **107**, 219 (1994).
20. T. A. Michtchenko and S. Ferraz-Mello, *Astron. Astrophys.* **303**, 945 (1995).
21. The three-body mean-motion resonances involve the mean motions of Jupiter, Saturn, and the asteroid, $\mathbf{n}_{Jup}$, $\mathbf{n}_{Sat}$ and $\mathbf{n}$, respectively, which obey the relation $k\mathbf{n}_{Jup} + l\mathbf{n}_{Sat} + m\mathbf{n} \sim 0$, where k, l, and m are integers (*23*, *24*).
22. D. Nesvorný and A. Morbidelli, *Astron. J.* **116**, 3029 (1998).
23. A. Morbidelli and D. Nesvorný, *Icarus* **139**, 295 (1999).
24. P. Farinella and D. Vokrouhlicky, *Science* **283**, 507 (1999).
25. ———, W. K. Hartmann, *Icarus* **132**, 378 (1998).
26. T. H. Burbine, thesis, Massachusetts Institute of Technology, Cambridge, MA (2000).
27. M. J. Gaffey, *J. Geophys. Res.* **81**, 905 (1976).
28. E. Bowell, K. Muinonen, L. H. Wasserman, *IAU Symp.* **160**, 477 (1994).

29. The Brazilian authors gratefully acknowledge the support of CNPq, Fundacão de Amparo à Pesquisa do Estado de São Paulo, Fundacão de Amparo à Pesquisa do Estado de Rio de Janeiro, and Fundacão Coordencão de Aperfeic de Pessoal de Nível Superior through diverse grants and fellowships and the Computation Center of the University State of São Paulo (LCCA-USP). The Massachusetts Institute of Technology portion of this research was supported by NASA grant NAG5-3939 and NSF grant AST-9530282.

23 February 2000; accepted 20 April 2000

Hierarchical Self-Assembly of F-Actin and Cationic Lipid Complexes: Stacked Three-Layer Tubule Networks

Gerard C. L. Wong,[1]* Jay X. Tang,[2]† Alison Lin,[1] Youli Li,[1] Paul A. Janmey,[2]‡ Cyrus R. Safinya[1]§

We describe a distinct type of spontaneous hierarchical self-assembly of cytoskeletal filamentous actin (F-actin), a highly charged polyelectrolyte, and cationic lipid membranes. On the mesoscopic length scale, confocal microscopy reveals ribbonlike tubule structures that connect to form a network of tubules on the macroscopic scale (more than 100 micrometers). Within the tubules, on the 0.5- to 50-nanometer length scale, x-ray diffraction reveals an unusual structure consisting of osmotically swollen stacks of composite membranes with no direct analog in simple amphiphilic systems. The composite membrane is composed of three layers, a lipid bilayer sandwiched between two layers of actin, and is reminiscent of multilayered bacterial cell walls that exist far from equilibrium. Electron microscopy reveals that the actin layer consists of laterally locked F-actin filaments forming an anisotropic two-dimensional tethered crystal that appears to be the origin of the tubule formation.

Self-assembly of amphiphilic molecules constitutes one of the most fundamental mechanisms for the construction of soft condensed matter materials. The distinct geometries adapted by lipids are typically described within a consistent framework of continuum elastic

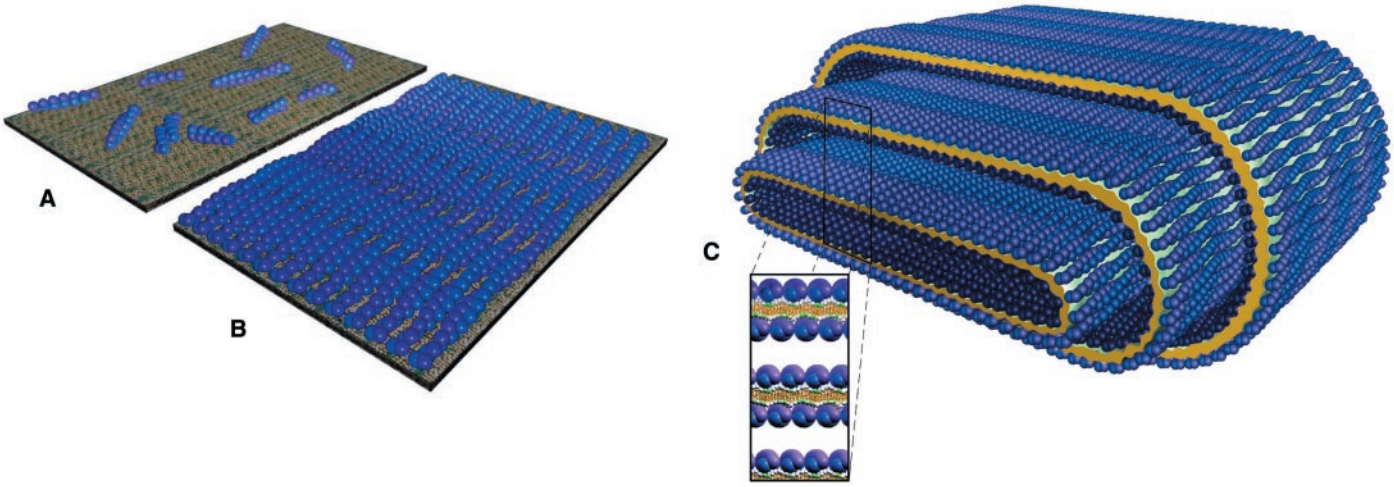

Fig. 1. Summary of the hierarchical self-assembly process resulting in the formation of ribbonlike tubules. (**A**) G-actin self-assembles into short F-actin filaments. (**B**) Long F-actin filaments spontaneously form a 2D crystal layer of F-actin. (**C**) The cationic lipid bilayer is sandwiched between two layers of F-actin, forming a three-layer membrane (inset), which folds into ribbonlike tubules.

models of membranes (*1–3*). The resulting structures include spherical and cylindrical micelles, bilayers, and inverse cylindrical micelles in cubic, hexagonal, lamellar, and inverted hexagonal phases. In certain rare cases not predicted by Helfrich's classical elastic theory of membranes (*4*), lipids self-assemble into cylindrical bilayers forming lipid tubules (*5–10*), multilamellar cylindrical vesicles (*11, 12*), and tubular cochleates (*13*). Although the mechanisms of tubule formation remain unknown, these novel systems continue to be increasingly used in technological applications, including drug and gene delivery systems (*14*), cosmetic formulations of gels and creams, and templates for processing microscale metal tubules for electronic and magnetic materials applications (*5–13*).

An alternate strategy for higher order self-assembly has been recently demonstrated: Interactions between biological polyelectrolytes and oppositely charged membranes can result in a complex polymorphism of new self-assembled architectures. For the DNA-membrane systems (currently used in nonviral gene delivery applications), this includes a lamellar phase (L^C_α) with DNA chains confined between lipid sheets (*15*) and an inverted hexagonal phase (H^C_{II}) with DNA contained within lipid tubes (*16*). In these systems, the cationic lipid head groups neutralize the phosphate groups on the DNA chains, so that condensed counterions on both macro-ions can be released for a large entropy gain (*17, 18*). Because the surface charge densities of DNA and cationic phospholipid head groups are similar, the counterion release is nearly maximal (*19*). However, if the surface charge densities of the two components are very different, as in the case of filamentous actin (F-actin) and cationic lipids, complete counterion release is sterically impossible. The resultant frustration is then expected to drive the system to new structures that are no longer constrained by typical geometries in amphiphilic self-assembly.

We report here the hierarchical self-assembly of actin and charged membranes elucidated at length scales ranging from nanometers to millimeters using synchrotron x-ray diffraction (XRD), freeze-fracture electron microscopy (EM), and laser scanning confocal microscopy. Interactions between uncharged membranes and actin have been known to result in deformed actin-membrane vesicles (*20, 21*). However, the entropically modulated electrostatic interactions between actin and charged membranes enforce a topological transition to a highly structured ribbonlike tubule morphology, with an average width of ~0.25 μm and a length of up to ~100 μm (Fig. 1). Globular monomeric actin (G-actin) polymerizes into F-actin filaments when complexed with charged membranes (Fig. 1A). Sufficiently long F-actin filaments further self-assemble into two-dimensional (2D) parallel arrays (Fig. 1B) electrostatically adsorbed on both sides of the cationic lipid bilayer forming a three-layer composite membrane (Fig. 1C, inset) with no direct analog in simple amphiphilic systems at equilibrium. The stacked composite membranes are folded into a compact, ribbonlike tubule structure with a nearly monodisperse mesoscale cross-sectional dimension of the order of 0.25 μm (Fig. 1C). Within the tubules, the composite membranes are osmotically swollen with a controllable water layer thickness ranging between 40 and 69 Å, which suggests that active molecules could be incorporated in these hydrated domains for drug and chemical delivery applications.

Actin is one of the principal structural proteins in eukaryotic cells and is an ideal biopolymer for investigations of new modes of higher order self-assembly. The actin cytoskeleton dynamically maintains the structural integrity of the plasma membrane and plays important roles in a number of membrane-associated events, such as cell adhesion, cell motility, and regulation of integral membrane protein distributions (*22*). This versatility is afforded by actin's ability to dynamically adjust its degree of polymerization from monomeric G-actin (~35 Å by 55 Å by 55 Å) to polymeric F-actin, which is essentially a polyampholytic helical hard rod. Although actin has a similar negative linear charge density compared to DNA ($\lambda_A \approx -2.5$ Å/e; $\lambda_{DNA} \approx -1.7$ Å/e), it has a much longer persistence length ($\xi_A \approx 10$ μm; $\xi_{DNA} \approx 500$ Å) and is larger in diameter ($D_A \approx 80$ Å; $D_{DNA} \approx 20$ Å). Its surface charge density is therefore considerably lower than that of typical cationic lipids (*19*). This charge density mismatch is expressed in the structure of actin-membrane complexes in unexpected ways.

Cationic lipids of three different chain

[1]Materials Department, Physics Department, and Biochemistry and Molecular Biology Program, University of California, Santa Barbara, CA 93106, USA. [2]Division of Experimental Medicine, Brigham and Women's Hospital, Harvard University, Boston, MA 02115, USA.

*Present address: Department of Materials Science and Engineering and Department of Physics, University of Illinois, Urbana-Champagne, IL 61801, USA.
†Present address: Department of Physics, Indiana University, Bloomington, IN 47405, USA.
‡Present address: Department of Physiology, Institute for Medicine/Engineering, University of Pennsylvania, Philadelphia, PA 19104, USA.
§To whom correspondence should be addressed. E-mail: safinya@mrl.ucsb.edu

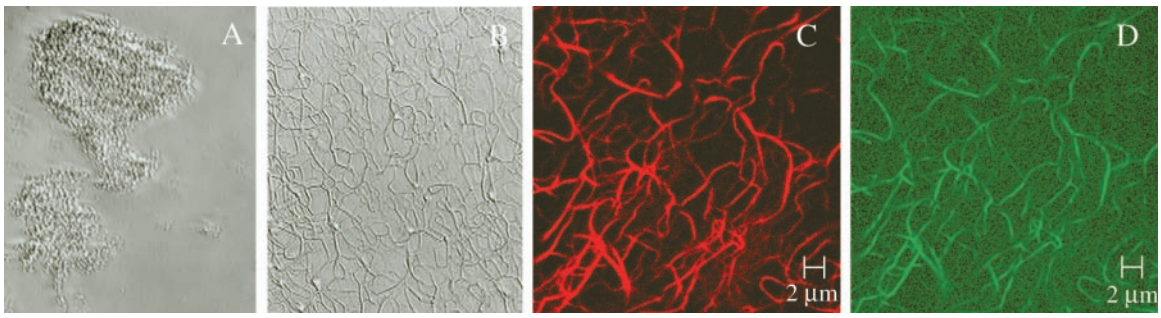

Fig. 2. Video-enhanced DIC microscopy images of (**A**) isoelectric G-actin membrane and (**B**) F-actin membrane complexes using DOTAP/DOPC = 50/50. The field of view is 50 μm by 65 μm. Laser scanning confocal images of F-actin complexes: (**C**) Texas red–labeled lipid and (**D**) coumarin green–labeled F-actin fluorescence.

lengths (C_{12}, C_{18}, and C_{24}) were used in this study: dilauryl-, dioleoyl-, and dinervonyltrimethyl ammonium propane (DLTAP, DOTAP, and DNTAP), respectively (Avanti Polar Lipids, Alabaster, Alabama). The membrane charge density was controlled by a neutral lipid dilution with a homologous lipid of the same chain length, but with the respective neutral phosphatidylcholine head group instead [dilauroyl phosphatidylcholine (DLPC), dioleoyl phosphatidylcholine (DOPC), and dinervonoyl phosphatidylcholine (DNPC)]. Liposome solutions (25 mg/ml) of the phospholipids were mixed thoroughly with the actin solution (*23*) to form the actin-membrane complexes. The relative charged membrane/actin stoichiometry of the complex is given by the ratio R, given in units of the isoelectric ratio R_{iso}, where the total charge of the membrane is equal and opposite to that of the actin. Here, $R_{iso} = L/A = 0.23$, where L is the weight of the charged lipid and A is the weight of actin.

The mesoscopic organizations of G-actin and F-actin membrane complexes are qualitatively different. Using video-enhanced optical microscopy with differential interference contrast (DIC), we found that G-actin complexes form globular aggregates at optical length scales (Fig. 2A) similar to those of DNA-membrane complexes (*15*). F-actin complexes, however, assemble into an ensemble of mesoscopic tubules with almost monodisperse diameters (~0.25-μm average width) (Fig. 2, B, C, and D). The tubules have lengths up to ~100 μm, which is much longer than the average lengths of the individual actin rods (~10 μm). Given the large persistence length of F-actin (~10 μm), the condensed actin rods within these tubules can only be parallel to the tubule axis. It must be emphasized that these tubules derive from the actin-membrane self-assembly and are not due to an ordering of the membrane phase alone: A confocal microscopy measurement of actin-membrane complexes made from fluorescently labeled actin (Fig. 2D) and lipids (Fig. 2C) shows that the two components are completely co-localized. Mechanical shearing can rupture the tubule network; however, the isolated tubules are robust and are very

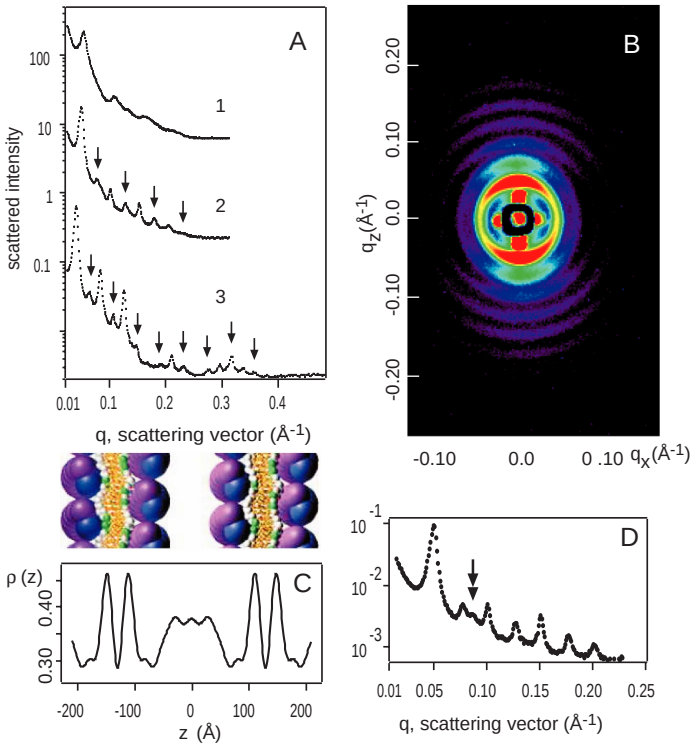

Fig. 3. Synchrotron XRD patterns from (**A**) isoelectric G-actin complexes using DOTAP/DOPC = 50/50 membranes (curve 1), isoelectric F-actin complexes using DOTAP/DOPC = 50/50 (curve 2), and F-actin complexes using DNTAP/DNPC = 30/70 on the positive side of the isoelectric point ($R = 2R_{iso}$). The superlattice peaks in the F-actin patterns (curves 2 and 3) are marked with arrows. (**B**) Two-dimensional x-ray diffraction pattern of a partially aligned DOTAP/DOPC = 30/70 sample shown on an image plate demonstrates the 1D superlattice ordering. (**C**) A ρ(z) electron density reconstruction of the unit cell, with a schematic representation of the composite actin-membrane-actin layers. The water layer is found to increase between 40 and 69 Å for DOTAP/DOPC varying between dilutions of 100/0 and 10/90. (**D**) Ultrahigh-resolution XRD showing the actin-actin correlation peak (double arrow) at the close-packing distance.

often found in the preparations coexisting with the network. Controlled shearing resulted in different average lengths for the tubules.

To investigate the molecular organization of these actin-membrane complexes, we performed a series of XRD experiments (*24*). A typical set of XRD data for isoelectric G-actin membrane (DOTAP/DOPC = 50/50) complexes is shown in Fig. 3A, curve 1. The four peaks in the diffraction pattern correspond to the (001) through (004) peaks of a one-dimensional (1D) lamellar structure with a period of 116 Å ($=2\pi/q_{001}$; $q_{001} = 0.054$ Å^{-1}). The thickness of the membrane in this case has been independently determined to be δ = 41 Å, which leaves ~75 Å as the gap for actin. This gap is inconsistent with the dimensions of monomeric G-actin (~35 or 55 Å, depending on orientation). This thickness, however, is approximately the diameter of polymerized F-actin ($D_A \approx 80$ Å). This result suggests that G-actin has polymerized into F-actin on the charged membrane surface without a polymerization buffer (Fig. 1A), as also suggested by observations on lipid surfaces (*25, 26*).

If long (~10 μm) F-actin instead of G-actin were complexed with the same charged membranes or if an excess of cationic lipids were added to G-actin, then something unexpected was observed. A new set of quasi-Bragg peaks appears near the half-integral positions of the corresponding peaks in G-actin complexes, so that nine orders of scattering can be readily observed (Fig. 3A, curve 2). In fact, the peaks at these half-integral positions (ar-

rows point to the peaks), which are detectable as weak peaks for some G-actin complexes [for example, Fig. 3A, curve 1, bump between (002) and (003)], gradually become stronger as the average F-actin filament length is increased (*27*). This behavior persists for the entire accessible range of neutral lipid dilution (DOTAP/DOPC = 100/0 to 10/90). Instead of a simple lamellar structure with a periodicity of $D_A + \delta$ (=116 Å), the actin-membrane system reconstructs into a lamellar superlattice with a periodicity of 250 Å, the precise value of which depends on the membrane charge density and thickness. The eight peaks in Fig. 3A, curve 2, correspond to the (002) through (009) higher harmonics of a 1D superlattice structure with $q_{001} = 0.025$ Å^{-1}. The form factor has a zero crossing near (001), resulting in a near extinction of the reflection. In the case of longer lipid chain DNTAP/DNPC complexes (Fig. 3A, curve 3), we observed up to 17 orders of diffraction from (002) through (017) of the 1D superlattice structure with periodicity of 299.2 Å ($q_{001} = 0.021$ Å^{-1}). In neutral lipid dilution experiments, where the membrane thickness was changed from 39 to 45 Å in DOTAP/DOPC complexes, we saw that these peaks all shift in unison as integral harmonics. The partially aligned diffraction pattern from a DOTAP/DOPC = 30/70 complex in Fig. 3B unambiguously demonstrates this 1D superlattice ordering.

To elucidate the structure of this polyelectrolyte-membrane superlattice phase, we performed an electron density reconstruction $\rho(z)$, where z is along the lamellar ordering direction. We compared the XRD data for isoelectric actin-membrane complexes with identical degrees of neutral lipid dilution (10/90) but with different membrane thicknesses, DOTAP/DOPC (C_{18}) and DLTAP/DLPC (C_{12}). The first- and third-order quasi-Bragg peaks in both actin-membrane complexes have weak intensities, indicating the proximity of form factor zero crossings. The form factor phases are determined from this "swelling" experiment using the Blaurock sum rule (*28, 29*) and are used to reconstruct $\rho(z)$. The results are shown in Fig. 3C. The membrane has a high average electron density near the phospholipid head groups (~0.46 e/Å^3) and a low density in the hydrocarbon tail region (~0.30 e/Å^3). Water has a density of 0.33 e/Å^3, and hydrated F-actin has an estimated density of ~0.27 e/Å^3. The location of the membrane layer can be found by inspection. The highest electron density coincides with the phospholipid head groups, and the low-density region between two adjacent head groups corresponds well with the expected thickness of the membrane (42 Å for DOTAP/DOPC; 33 Å for DLTAP/DOPC) (Fig. 3C, top). On either side of each membrane, there exists a region ~80 Å thick, equal to the diameter of F-actin and with a low density that is consistent with the existence of F-actin. The region of intermediate electron density between the actin is a water layer with thickness near 50 Å. By normalizing $\rho(z)$ with densities for lipid head and tail groups, we find a densities of 0.37 e/Å^3 for the water layer (which contains counterions) and 0.30 e/Å^3 for the F-actin layers, which are consistent with the expected values.

The XRD data show that the superlattice structure consists of a three-layer membrane. Compared to the DNA-membrane phases (*15*), this superlattice structure accommodates two layers of F-actin rods per membrane sheet (rather than the one layer of DNA per membrane), which is consistent with the charge density mismatch (*19*). However, although for a lamellar geometry of the lipids, this three-layer configuration is more favorable than the two-layer DNA-membrane configuration, but it still does not result in a perfect match of anionic and cationic charge densities of the macro-ions. Thus, local charge neutrality will require a finite anionic counterion concentration in the aqueous region between membranes, which then gives rise to the osmotically swollen nature of the tubule measured by XRD (*30*).

To explore the nature of the F-actin layer, we imaged the complexes with freeze-fracture EM, which revealed a locked 2D actin lattice within these mesoscopic tubules (Fig. 4). An ensemble of flattened multilamellar tubules can be seen, with an average width of ~0.25 μm, in agreement with the optical microscopy measurements. Moreover, a surface corrugation along the axis of the tubules with a periodicity of 35 nm can be discerned on the fracture plane. This value corresponds to the long-wavelength twist native to F-actin. The existence of well-defined corrugations across a layer suggests that the actin filaments are laterally locked into 2D arrays within each layer, with the filaments oriented along the axis of the tubules. Because the fracture plane is in the middle of the lipid bilayer, the lipid molecules themselves must be corrugated on the surface of F-actin (*31*). It can also be seen from Fig. 4 that the phase of this long-wavelength corrugation is not preserved across adjacent layers, in contrast to the direction of the wave vector, which is always directed along the tubule axis. This result suggests that the positional correlations between the 2D actin rods in adjacent layers can be lost without destroying the orientational correlations. Recent theoretical work predicts the possible existence of a sliding phase in stacks of 2D crystals with similar properties (*32*). An ultrahigh-resolution XRD experiment (*24*) on actin-membrane complexes clearly demonstrates the first-order actin-actin correlation peak at $d = 75$ Å (Fig. 3D, double arrow) in the DOTAP/DOPC = 30/70 sample. This value of d is equal to the F-actin hard-core diameter and implies that the F-actin rods have fully condensed into this 2D locked lattice within the complex, consistent with the EM data. Interestingly, the outermost layer of bacterial cell walls is known to consist of 2D crystals, the so-called surface (S) layer, usually composed of a self-assembly of a single type of glycoprotein (*33*).

In contrast to the 1D DNA lattice in DNA-membrane complexes (*15*), which is dominated by repulsive interactions between the chains, the locked 2D actin lattice is the result of an attractive interaction. In three dimensions, actin rods can condense into bundles or paracrystals in the presence of a high enough concentration of divalent (and higher multivalent) ions (*34–37*). However, in the 2D environment of the actin-membrane complex, monovalent cationic lipids alone can condense actin rods into a lattice without multivalent ions.

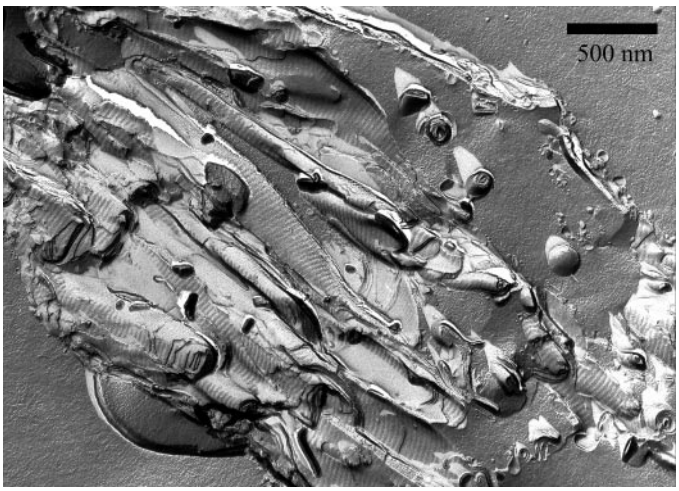

Fig. 4. Freeze-fracture EM of ribbonlike tubules. The 35-nm corrugations along the length of the flattened tubules correspond to the long-wavelength twist of F-actin. The persistence of these corrugations across the widths of the tubules suggest that the F-actin rods on the membrane are locked into a 2D lattice.

This condensation process may be mediated in part by membrane distortions, which results in an effective attractive interaction because actin aggregation minimizes the perturbed membrane area (*38*).

The formation of ribbonlike tubules from 2D actin-membrane sheets may be related to the physics of crystalline membranes (*39*–*42*). Linear polymer chains adopt a "crumpled" random coil conformation in a good solvent. The behavior for a 2D polymer sheet, however, is dramatically different. In these so-called "tethered membranes," thermal undulations are coupled to phonon modes, which can stiffen the membrane at large length scales, leading to an infinite persistence length. The resultant low-temperature "flat phase" has been observed (*43*). Figure 4 demonstrates that the actin rods are ordered into 2D anisotropic lattices on charged membranes and thereby form composite anisotropic tethered membranes. Repulsive "self-avoiding" steric interactions are inherently less constraining for systems that crumple in one direction only. In the case of oriented actin-membrane sheets, the large persistence length of actin will completely prevent crumpling along the rod direction, whereas the attractive interaction between actin rods may counterbalance the steric interactions and lead to the tubule phase consistent with the prediction of theory for anisotropic tethered membranes (*44*–*46*). This intrinsic tendency of anisotropic crystalline membranes to curl up into tubules will impinge on the structure of paracrystalline sheets constrained to a flat 2D surface and may place fundamental limits on the 2D crystallography of these objects.

We have described a form of self-assembly based on entropically modulated electrostatic interactions, which leads to the formation of a ribbonlike tubule phase stabilized by a three-layer (actin–lipid bilayer–actin) membrane. The governing concepts for this biological self-assembly are general; for example, we expect synthetic analogs, such as charged polymersomes of diblock copolymers (*47*) and polyelectrolytes, to give rise to similar complex membrane architectures and "plastic" tubules for chemical delivery and a variety of other applications. Finally, we note that although eubacteria and archaebacteria construct composite envelopes containing between two and four layers, the directed assembly is far from equilibrium and requires adenosine 5′-triphosphate (ATP) hydrolysis (*33*). The tubules described here with their composite membrane architecture can be thought of as constituting a spontaneously assembled "artificial" bacterium.

References and Notes

1. W. M. Gelbart, A. Ben-Shaul, D. Roux, Eds., *Micelles, Membranes, Microemulsions, and Monolayers* (Springer-Verlag, New York, 1994).
2. S. A. Safran, *Statistical Thermodynamics of Surfaces, Interfaces, and Membranes* (Addison-Wesley, Reading, MA, 1994).
3. R. Lipowsky and E. Sackmann, Eds., *Structure and Dynamics of Membranes* (Elsevier Science, New York, 1995).
4. W. Helfrich, *Z. Naturforsch. C* **28**, 693 (1973).
5. J. M. Schnur, *Science* **262**, 1669 (1993).
6. M. S. Spector, R. R. Price, J. M. Schnur, *Adv. Mater.* **11**, 337 (1999).
7. R. Oda, I. Huc, M. Schmutz, S. J. Candau, F. C. MacKintosh, *Nature* **399**, 566 (1999).
8. B. N. Thomas, C. R. Safinya, R. J. Plano, N. A. Clark, *Science* **267**, 1635 (1995).
9. B. N. Thomas *et al.*, *J. Am. Chem. Soc.* **120**, 12178 (1998).
10. B. N. Thomas, C. M. Lindemann, N. A. Clark, *Phys. Rev. E* **59**, 3040 (1999).
11. S. Chiruvolu *et al.*, *Science* **266**, 1222 (1994).
12. B. Klosgen and W. Helfrich, *Eur. Biophys. J.* **22**, 340 (1993).
13. D. Papahadjopoulos *et al.*, *Biochim. Biophys. Acta* **394**, 483 (1975).
14. D. D. Lasic, *Liposomes in Gene Delivery* (CRC Press, Boca Raton, FL, 1997).
15. J. O. Rädler, I. Koltover, T. Salditt, C. R. Safinya, *Science* **275**, 810 (1997).
16. I. Koltover, T. Salditt, J. O. Rädler, C. R. Safinya, *Science* **281**, 78 (1998).
17. R. Bruinsma, *Eur. Phys. J. B* **4**, 75 (1998).
18. D. Harries, S. May, W. Gelbart, A. Ben Shaul, *Biophys. J.* **75**, 159 (1998).
19. The projected charge density of DNA (two anionic charges per 68 Å^2) is nearly matched by the cationic head groups of two DOTAP molecules, with area of ~70 Å^2, above and below the DNA rod in the lamellar complex and permits near complete neutralization. F-actin has a charge density that is at least four times less than that of DNA.
20. W. Häckl, M. Bärmann, E. Sackmann, *Phys. Rev. Lett.* **80**, 1786 (1998).
21. H. Miyata, S. Nishiyama, K.-I. Akashi, K. Kinosita, *Proc. Natl. Acad. Sci. U.S.A.* **96**, 2048 (1999).
22. H. Lodish *et al.*, *Molecular Cell Biology* (Freeman, New York, ed. 4, 1999).
23. Monomeric G-actin (molecular weight of 43,000) was prepared from an acetone powder of rabbit skeletal muscle. The nonpolymerizing G-actin solution contained a 4 mM Hepes buffer at pH 7.2, with 0.2 mM $CaCl_2$, 0.5 mM ATP, and 0.5 mM NaN_3. G-actin (2 mg/ml) was polymerized into F-actin with the addition of salt (100 mM KCl). The filaments were then treated with phalloidin (molecular weight of 789) to prevent actin depolymerization. F-actin gels were ultracentrifuged at 100,000*g* to pellet the filaments, which typically have a mean length of several micrometers. After the removal of the supernatant buffer solution, the F-actin was diluted to a final concentration of 10 mg/ml using Millipore H_2O (18.2 megohms). Human plasma gelsolin, purified by elution from a DE-52 ion-exchange matrix in 30 mM NaCl, 3 mM $CaCl_2$, and 25 mM tris at pH 7.4 was used to regulate the mean F-actin length in length-dependence studies.
24. XRD experiments were performed at beamlines 7-2 and 10-2 of the Stanford Synchrotron Radiation Laboratory. The x-ray energy was monochromatized to 10 keV using a double-bounce Si(111) crystal at both beamlines. The incoming beam was focused with a bent cylindrical mirror and had a horizontal divergence of ~2 mrad [out-of-plane resolution of ~0.01 Å^{-1}, half width at half maximum (HWHM)]. Resolution in the vertical scattering plane was set to 0.0031 Å^{-1} (HWHM) using slits. Ultrahigh-resolution XRD was carried out with a Si(111) analyzer to increase the in-plane resolution to 1.3×10^{-4} Å^{-1} (HWHM). The actin-membrane complex samples are sealed in 1.5-mm quartz capillaries.
25. A. Laliberte and C. Gicquaud, *J. Cell Biol.* **106**, 1221 (1988).
26. A. Renault *et al.*, *Biophys. J.* **76**, 1580 (1999).
27. If we restrict the F-actin filaments to an average length of 500 Å with gelsolin, an actin severing and capping protein, then the superlattice ordering is suppressed in the resultant actin-membrane complexes.
28. A. E. Blaurock, *J. Mol. Biol.* **56**, 35 (1971).
29. N. P. Franks, T. Arunachalam, E. Caspi, *Nature* **276**, 530 (1978).
30. Although the F-actin cationic lipid complexes always show the superlattice peaks resulting from stacked three-layer membranes, the XRD from G-actin complexes show only hints of the superlattice ordering. This may be due to the coexistence of two-layer G-actin complexes (with alternating lipid bilayer and G-actin monolayers) with a very small fraction of the G-actin that has polymerized into very long F-actin, forming the three-layer membrane. Because G-actin (or very short F-actin) does not contain any condensed counterion because of its globular shape (or extreme finite size for short F-actin), G-actin attached to cationic membrane releases only the bound counterions of the membrane. In the process, G-actin lowers its own entropy (which is negligible for long F-actin) and reduces some of the entropy of the lipids [by their ordering on its surface as suggested by the EM freeze-fracture and molecular dynamics simulations studies (*31*)]. Thus, there is a delicate balance between how much entropy is gained each time G-actin attaches a membrane and releases anionic lipid counterions and the entropy lost because of the lipid ordering on the G-actin surface. In the case of long F-actin, the situation is very different because an additional large amount of bound cationic counterions is also released upon complexation. Thus, for G-actin complexes, a two-layer membrane may be entropically more favorable than a three-layer membrane. Alternatively, G-actin complexes composed of three-layer membranes with antiphase-type defects would tend to wash out the superlattice peaks.
31. S. Bandyopadhyay, M. Tarek, M. L. Klein, *J. Phys. Chem. B* **103**, 10075 (1999).
32. C. S. O'Hern, T. C. Lubensky, J. Toner, *Phys. Rev. Lett.* **83**, 2745 (1999).
33. M. Sara and U. B. Sleytr, *Prog. Biophys. Mol. Biol.* **65**, 83 (1996).
34. J. X. Tang and P. A. Janmey, *J. Biol. Chem.* **271**, 8556 (1996).
35. J. Hanson, *Proc. R. Soc. London Ser. B* **183**, 39 (1973).
36. L. Rioux and D. Gicquaud, *J. Ultrastruct. Res.* **93**, 42 (1985).
37. K. A. Taylor and D. W. Taylor, *J. Struct. Biol.* **108**, 140 (1992).
38. N. Dan, *Biophys. J.* **71**, 1267 (1996).
39. D. R. Nelson, T. Piran, S. Weinberg, Eds., *Statistical Mechanics of Membranes and Interfaces* (World Scientific, Singapore, 1989).
40. Y. Kantor and D. R. Nelson, *Phys. Rev. Lett.* **57**, 791 (1986).
41. F. F. Abraham and D. R. Nelson, *Science* **249**, 393 (1990).
42. J. A. Aronovitz and T. C. Lubensky, *Phys. Rev. Lett.* **60**, 2634 (1988).
43. C. F. Schmidt *et al.*, *Science* **259**, 952 (1993).
44. L. Radzihovsky and J. Toner, *Phys. Rev. Lett.* **75**, 4752 (1995).
45. M. Bowick, M. Falcioni, G. Thorleifsson, *Phys. Rev. Lett.* **79**, 885 (1997).
46. M. Bowick and A. Travesset, *Phys. Rev. E* **59**, 5659 (1998).
47. B. M. Discher *et al.*, *Science* **284**, 1143 (1999).

48. We thank R. Golestanian, I. Koltover, R. Menes, P. Pincus, and D. Roux for discussions. In particular, we acknowledge L. Zarif for discussions on the EM work. This work was supported by NIH grants GM59288 and AR38910, NSF grant DMR-9972246, the Cystic Fibrosis Foundation (grant 00G0), and the University of California Biotechnology Research and Education Program (grant 99-14). The Materials Research Laboratory at University of California at Santa Barbara is supported by NSF grants DMR-9632716 and DMR-0080034.

17 February 2000; accepted 3 May 2000